Nanoscale Advances

ROYAL SOCIETY OF CHEMISTRY

PAPER

View Article Online
View Journal | View Issue

Cite this: *Nanoscale Adv.*, 2023, **5**, 3396

Physicochemical properties of different crystal forms of manganese dioxide prepared by a liquid phase method and their quantitative evaluation in capacitor and battery materials

Yang Pan, †[ac] Wang Jiawei,†[abc] Wang Haifeng,†*[abc] Wang Song,[ac] Yang Chunyuan[ac] and He Yue[ac]

Although there are many studies on the preparation and electrochemical properties of the different crystal forms of manganese dioxide, there are few studies on their preparation by a liquid phase method and the influence of their physical and chemical properties on their electrochemical performance. In this paper, five crystal forms of manganese dioxide were prepared by using manganese sulfate as a manganese source and the difference of their physical and chemical properties was studied by phase morphology, specific surface area, pore size, pore volume, particle size and surface structure. The different crystal forms of manganese dioxide were prepared as electrode materials, and their specific capacitance composition was obtained by performing CV and EIS in a three-electrode system, introducing kinetic calculation and analyzing the principle of electrolyte ions in the electrode reaction process. The results show that δ-MnO_2 has the largest specific capacitance due to its layered crystal structure, large specific surface area, abundant structural oxygen vacancies and interlayer bound water, and its capacity is mainly controlled by capacitance. Although the tunnel of the γ-MnO_2 crystal structure is small, its large specific surface area, large pore volume and small particle size make it have a specific capacitance that is only inferior to δ-MnO_2, and the diffusion contribution in the capacity accounts for nearly half, indicating it also has the characteristics of battery materials. α-MnO_2 has a larger crystal tunnel structure, but its capacity is lower due to the smaller specific surface area and less structural oxygen vacancies. ε-MnO_2 has a lower specific capacitance is not only the same disadvantage as α-MnO_2, but also the disorder of its crystal structure. The tunnel size of β-MnO_2 is not conducive to the interpenetration of electrolyte ions, but its high oxygen vacancy concentration makes its contribution of capacitance control obvious. EIS data shows that δ-MnO_2 has the smallest charge transfer impedance and bulk diffusion impedance, while the two impedances of γ-MnO_2 were the largest, which shows that its capacity performance has great potential for improvement. Combined with the calculation of electrode reaction kinetics and the performance test of five crystal capacitors and batteries, it is shown that δ-MnO_2 is more suitable for capacitors and γ-MnO_2 is more suitable for batteries.

Received 6th March 2023
Accepted 5th May 2023

DOI: 10.1039/d3na00144j

rsc.li/nanoscale-advances

1 Introduction

MnO_2 is often used in the field of electrochemistry because it has good electronic properties, transfers protons and electrons easily, and undergoes reversible redox reactions. It can not only be used as a typical pseudocapacitive material[1–3] but also as a raw material for synthesizing lithium manganate as a battery cathode material.[4,5] With respect to supercapacitors, manganese dioxide has the advantages of large theoretical specific capacity, wide potential window, easy realization of fast reversible redox reaction, simple synthesis process, low cost and environmental protection. It has become the most promising electrode material to replace RuO_2.[6–9] Manganese oxide can be used as a manganese source for synthesizing lithium manganate. Manganese dioxide is often studied and compared with manganese tetroxide and manganese salicylate sesquioxide.[10–14] Although manganese dioxide has been extensively studied as a precursor material of capacitors and lithium manganate, due to the fact that manganese dioxide has a variety of crystal forms, different crystal forms cause different electrochemical

[a]College of Materials and Metallurgy, Guizhou University, Guiyang, 550025, China. E-mail: 571012350@qq.com; 67749951@qq.com

[b]Engineering Technology and Research Center of Manganese Material for Battery, Tongren, 554300, China. E-mail: 380889450@qq.com; 1689170027@qq.com

[c]Guizhou Key Laboratory of Metallurgical Engineering and Process Energy Conservation, Guiyang, 550025, China. E-mail: 475761730@qq.com; 2975185501@qq.com

† These authors contributed equally to this work.

properties, and there were different performances in capacitors and battery materials. Therefore, it is of great significance to determine the electrochemical reaction mechanism of different forms of manganese dioxide and to further determine their use directions respectively.

There have been many reports on the preparation of MnO_2,[15–17] such as *via* the traditional hydrothermal method, template method, co-precipitation method, solid phase method, novel ultrasonic method and microwave method in recent years. The hydrothermal method[18–26] can achieve uniform and controllable crystal growth. The products prepared have good morphology, crystallinity and dispersion, complete crystal form, and controllable crystal size. However, due to the need to maintain a high temperature and high pressure synthesis environment, it is more complex than other synthesis methods. Template preparation of manganese dioxide is simple, but other impurities were easy to be introduced when removing the template, which affects the purity of the final production.[27] The sol–gel method is often combined with the template method. The products prepared by this method have uniform dispersion and high purity, but the reaction period is long and the calcination process will produce agglomeration.[28,29] The solid-phase synthesis method is a simple, efficient and low-cost method because of its simple experimental method, less environmental pollution, high product yield and good reaction selectivity. However, manganese dioxide is sensitive to grinding, temperature and other test conditions, so the product purity is low and it easily agglomerates.[30,31] The microwave method of preparing MnO_2 has the advantages of uniform heating of reactants, fast reaction speed, high yield, high selectivity and environmental protection, but it also needs to heat the microwave reactor in the microwave device.[32,33] Compared with the above manganese dioxide synthesis method, the product prepared by the chemical precipitation method[34–36] has poor particle uniformity, easy agglomeration, poor crystallinity, *etc.* But the manganese dioxide prepared by the chemical precipitation method has high purity, the method has low reaction temperature, low energy consumption, safe and simple operation, simple equipment, low cost, *etc.* Therefore, in this study, the chemical precipitation method was selected. After consulting a large number of methods for preparing different crystal forms of manganese dioxide,[37–42] direct or indirect preparation of different crystal forms of manganese dioxide at low temperature in a liquid environment was attempted.

The electrochemical performance of MnO_2 as an electrode material has been extensively studied. The theoretical specific capacitance of MnO_2 is 1370 F g^{-1}, but the actual specific capacitance is much lower than this value.[43] The main reasons for this are its own physical and chemical properties and electrolyte type. The morphology, specific surface area, pore size, intrinsic conductivity, crystal structure, interlayer bound water and crystal form of manganese dioxide will affect its electrochemical performance.[8,9,44,45] Shen B. S.[7] prepared manganese dioxide with four different morphologies, and they are nanorods, nanospheres, hollow nanospheres and nanosheets. The comparative study results show that the specific capacitance of the nanosheet manganese dioxide electrode material is the largest, reaching 96.5 F g^{-1}. The larger specific surface area of manganese dioxide can provide more redox active sites, shorten the diffusion path and increase the contact area with electrolyte ions. The appropriate pore size can increase the accessibility of ions.[46–48] In order to improve the conductivity of manganese dioxide, graphene and carbon nanotubes can be added into it, or MnO_2 can be loaded onto a conductive substrate to create more contact interfaces, so as to improve charge transfer efficiency.[49–52] Doping different atoms and materials,[53–56] forming heterostructures between different crystal forms,[57–59] and intercalating ions between layers can modify the manganese dioxide crystal structure,[60–62] which can improve the conductivity and increase the layer spacing, thus improving the electrochemical performance. The existence of oxygen vacancy promotes charge transfer in the local electric field and improves the surface redox reaction kinetics and the conductivity, thus improving the electrochemical performance.[63,64] Different crystal forms of MnO_2 have different crystal structures, microstructures, specific surface areas, pore size distributions, surface structures, oxygen vacancies, and surface hydroxyl groups, which directly lead to differences in electrochemical performance. In this study, the above performance parameters of the five crystal forms of manganese dioxide were compared by the corresponding characterization methods. The common electrolytes are divided into acidic,[65] neutral, and alkaline.[66] Neutral electrolyte is the mainstream, which mainly includes different concentrations of $NaNO_3$, Na_2SO_4, Li_2SO_4 and other salt solutions.[67,68]

Electric double layer capacitance is a pure physical process[69,70] and is generated by the formation of charged double layers at the electrode–electrolyte interface due to ion migration in the electrolyte. The pseudocapacitor contains both the capacity generated by the electric double layer and the capacity generated by the rapid charge storage of the redox reaction, and the latter makes the main capacity contribution. The redox reactions in the pseudocapacitor include three mechanisms; they are underpotential deposition, rapid redox reactions occurring near and on the surface of materials and ion intercalation.[71–75] The capacity of MnO_2 in neutral electrolyte comes from electric double layer capacitance and pseudocapacitance, and the contribution of pseudocapacitance mainly comes from two aspects.[76,77] On one hand, it mainly depends on the contribution of surface redox reaction. On the other hand, it comes from the intercalation–deintercalation redox reaction of cations in MnO_2. Most pseudocapacitor researchers believe that the capacity contribution only comes from the redox reaction of Mn^{3+}/Mn^{4+} on the surface and subsurface of the MnO_2 material, and the capacity contribution of the ion intercalation redox reaction is not clear. There are few studies on the specific proportion of surface and bulk redox reactions in the capacity contribution of the five crystal forms.

In this paper, five crystal forms of manganese dioxide were prepared by a liquid phase method, then their physical and chemical properties were studied and the influence of their physical and chemical properties on electrochemical performance was analyzed. The CV and EIS curves of different crystal

form manganese dioxide electrodes were measured in a three-electrode system, and the specific capacitance and impedance were obtained. Through the calculation of electrode kinetics, the capacitance contribution of the five crystal forms of manganese dioxide was distinguished, and the use direction of the material was determined. It was used as a capacitor material and a battery material to verify the performance under constant current charge and discharge, and the applicability of different crystal forms of manganese dioxide prepared by liquid phase synthesis in the direction of use was determined again, which provided an alternative to electrolytic preparation.

2 Experimental

2.1 Experimental reagents and equipment

The experimental reagents are analytically pure reagents. The manganese sulfate, ammonium persulfate, sodium hydroxide, potassium permanganate, and ammonium bicarbonate used in the experiment are produced by State Pharmaceutical Group Chemical Reagent Co., Ltd. Hydrogen peroxide with 30% concentration and 98% sulfuric acid are produced by East Sichuan Chemical Industry.

Experimental equipment is as follows. The constant temperature water bath (HH-3) is produced by Shanghai Kexi Experimental Instrument Factory. The constant temperature drying oven (DHG-9005A) is produced by Beijing Yongguangming Medical Instrument Factory. The vacuum suction filter pump (P4Z) is produced by Beijing Jinghui Kaiye Co., Ltd, the electronic analytical balance (PL2002) is produced by Mettler-Toledo Instruments (Shanghai) Co., Ltd, the precision booster electric stirrer (JJ-1) is produced by Changzhou Aohua Instrument Co., Ltd, the box resistance furnace (SX-4-10) is produced by Tianjin Taisite Scientific Instrument Co., Ltd.

2.2 Experimental process

2.2.1 Preparation of the five crystal forms of MnO_2. 500 ml manganese sulfate solution with a manganese ion concentration of 30 g L^{-1} was prepared with deionized water. 62.30 g ammonium persulfate was weighed and dissolved in 500 ml deionized water to ensure that the ratio of manganese ion to ammonium sulfate was 1 : 1. The manganese sulfate solution was heated to 80 °C in a water bath, and the prepared ammonium persulfate solution was added by dropping. At the same time, the solution was stirred at 300 rpm. After 6 hours, a black sediment was obtained by filtration. It was washed with deionized water many times, then dried at 110 °C in an air blast oven and ground with an agate mortar to obtain α-MnO_2.

500 ml manganese sulfate solution and 500 ml sodium hydroxide solution were prepared with deionized water. Manganese ion concentration was 30 g L^{-1}, and sodium hydroxide concentration was 30 g L^{-1}. When the stirring speed was 400 rpm, $MnSO_4$ was added drop by drop into the sodium hydroxide solution, and the pH value of the reaction solution was continuously measured. When the pH value was close to neutral, the addition of manganese sulfate solution was stopped, and the volume of added manganese sulfate was read. The molar ratio of manganese ion and hydrogen peroxide was controlled to be 1 : 1. The hydrogen peroxide was slowly added to the reaction solution drop by drop. After 2 h of reaction, H_2SO_4 was slowly added to adjust the pH value to 2. After 1 h of reaction, the reaction solution was vacuum filtered. The filter residue was taken out after 12 h of drying in an oven at 110 °C and ground with an agate mortar to obtain γ-MnO_2.

The γ-MnO_2 prepared in this experiment was put into a ceramic crucible, and then put into a muffle furnace. After slowly heating up to 400 °C in an air atmosphere for 4 h, the power was turned off, and the sample was naturally cooled to room temperature to obtain β-MnO_2.

Manganese sulfate solution and potassium permanganate solution were prepared with deionized water, with manganese ion concentration of 30 g L^{-1} and potassium permanganate concentration of 30 g L^{-1}. 500 ml potassium permanganate solution was placed in a beaker and heated to 80 °C in a water bath pan, and then manganese sulfate solution was added into it. The ratio of manganese ions in manganese sulfate to those in potassium permanganate was 1 : 1.5, maintaining excessive potassium permanganate. During the reaction, the magnetic rotor was used for stirring. Six hours after the reaction, the precipitate was filtered, dried, and ground in an agate mortar to obtain δ-MnO_2.

500 ml manganese sulfate solution with a manganese ion concentration of 30 g L^{-1} was prepared with deionized water. 43.14 g ammonium bicarbonate was dissolved in 500 ml deionized water. The ammonium bicarbonate solution was added to the manganese sulfate solution and it was continuously stirred. After the reaction was completed, the solution was filtered to obtain the filter residue, which was put into the oven for drying. After that, the filter residue was ground into powder to obtain manganese carbonate. Then, the manganese carbonate was put into a ceramic crucible and transferred to the muffle furnace for burning for 4 h at 400 °C, after which ε-MnO_2 was obtained.

2.2.2 Preparation of a pseudocapacitive electrode sheet. The mass ratio of manganese dioxide, acetylene black and PTFE was controlled at 7 : 2 : 1. 0.07 g manganese dioxide, 0.02 g acetylene black and 115 μl (about 0.01 g) PTFE and 400 μl deionized water were weighed and put into the agate mortar, and a slurry was prepared by fully grinding the mixture. Then the nickel foam with thickness of 0.3 mm was cut into a 1 × 2 cm^2 piece and its mass was weighed. Fully ground slurry is coated on the current collector and it was ensured that the coating area was 1 × 1 cm^2. Next, the coated pole piece was placed on the glass plate and transferred to the oven at 110 °C, the pole piece was taken out after 12 h and was pressed with a pressure of 10 MPa, and the amount of active material loaded was calculated and recorded. The prepared electrode was tested in a three-electrode system composed of an electrode clamp, platinum electrode and saturated calomel electrode. The electrolyte was 1 mol L^{-1} Na_2SO_4 solution. The voltage range of the CV curve was 0–1 V in a three-electrode system, and the impedance was tested by EIS in the frequency range of 10^{-2}–10^6 Hz. The charge–discharge long cycle test of the electrode was carried out on a Xinwei battery system. The charging voltage

was 1.0 V, the discharge voltage was 0.01 V, and the current density was 0.1 A g^{-1}.

2.2.3 Synthesis of the battery cathode material and preparation of the cathode sheet. $LiMn_2O_4$ was synthesized by a high-temperature solid-phase method. The molar ratio of manganese dioxide to lithium hydroxide was 1.02 : 2, the amount of lithium hydroxide was 0.24429 g and manganese dioxide was 1.7388 g. The two were poured into the mortar and ground for half an hour to fully integrate them, then the mixed samples were transferred to an alumina crucible, and placed in the muffle furnace for roasting. $LiMn_2O_4$ was obtained when the reaction was done at 800 °C for 7 h and cooled to room temperature.

The lithium half battery assembly process was as follows. Firstly, 0.3 g PVDF was dissolved in 10 ml NMP, and magnetic stirring was performed for 12 h. 0.08 g lithium manganate, 0.01 g acetylene black and 0.01 g (about 333 μL) PVDF were put into the mortar and ground for 3 min to ensure full integration. Secondly, the carbon aluminum foil was fixed on the glass plate, and the mixed slurry was coated on it by using a tetragonal preparator. And it was dried at 110 °C in the vacuum oven. After 12 h, it was taken out and was cut into a circular disc with a diameter of 1 cm with a cutting machine. The active substance was calculated by weighing the quality of the pole piece. Thirdly, the electrode was transferred to a glovebox to assemble the lithium half-cell. The lithium half-cell was assembled in the order of negative electrode shell, lithium sheet, electrolyte (35 μL), diaphragm, electrolyte (35 μL), positive electrode sheet, gasket, shrapnel and positive electrode shell. The assembled half-cell was packaged with a battery packaging machine at a pressure of 10 MPa. Finally, the charge and discharge cycle test of 1C was done using a Xinwei battery test system, and the charge and discharge section was 3–4.3 V.

2.2.4 Electrochemical calculation. According to the polarization position of manganese dioxide and the aqueous electrolyte sodium sulfate, when the voltage window is 0–1 V, the specific capacitance was calculated by the CV curve. The calculation formula is as follows:

$$C_p = \frac{\int_{V_1}^{V_2} I(V)\mathrm{d}V}{2vm(V_2 - V_1)} = \frac{A}{2vm(V_2 - V_1)} \quad (1)$$

where v is the scanning rate (V s^{-1}), m the loading mass of the active substance (g), $V_2 - V_1$ the potential window (V), A the area enclosed by the CV curve, and C_p the specific capacitance of the electrode material (F g^{-1}).

In the electrode dynamics process, qualitative calculation was done using Formula (2) and quantitative calculation was done using Formula (3) (ref. 78)

$$i = av^b \quad (2)$$

where i is the peak current (A), v is the scan rate (V s^{-1}), and a and b are constants.

$$i(V) = k_1 v + k_2 v^{0.5} \quad (3)$$

where i is the peak current (A), v is the scan rate (V s^{-1}), and $k_1$and k_2 are constants.

2.3 Analytical methods

In the experiment, the phase was identified using a BRUKER D8 ADVANCE diffraction analyzer of Bruker company in Germany. The microstructure was analyzed using an SU8020 scanning electron microscope of Hitachi company in Japan. The FT-IR analysis was performed on an IS10 FT-IR spectrometer produced by Nicolet company in the United States, and the XPS data was collected on a Thermo Escalab 250Xi electron spectrometer produced by Mercury Technology in the United States. The specific surface area, pore volume and pore size were measured using a Mike ASAP 2460 physical adsorption instrument. Electrochemical tests of CV and EIS were performed using a CHI604E electrochemical workstation produced by Shanghai Chenhua Instrument Co., Ltd, and constant current charge and discharge were tested using a CT-4008Tn-5V 20mA-164 produced by Guangdong Xinweier Electronics Co., Ltd.

3 Characterization and analysis of basic physicochemical properties

3.1 Phase and micro-morphology

The XRD patterns of the five crystal forms of manganese dioxide are shown in Fig. 1. The crystal form was determined by comparing them with the standard PDF cards. The peak positions at 12°, 18°, 28°, 38°, 42°, 56°, 60°, and 66° are consistent with the JCPDS 72-1982 standard card of α-MnO_2. The peak positions at 28°, 37°, 42°, 56°, and 72° are consistent with the JCPDS 24-0735 standard card of β-MnO_2. The peak positions at 22°, 37°, 42°, 56°, and 67° are consistent with the JCPDS 44-0142 standard card of γ-MnO_2. The peak positions at 12°, 24°, 38°, and 66° are consistent with the JCPDS 44-1386 standard card of δ-MnO_2, and the peak position was at 12°, which is mainly caused by K^+. The peak positions at 37°, 43°, 57°, and 67° are consistent with the JCPDS 30-0820 standard card of ε-MnO_2. The preparation was liquid phase synthesis, and the reaction is not in the high pressure environment. Therefore, it can be seen from Fig. 1 that the crystallinity of the five manganese dioxide

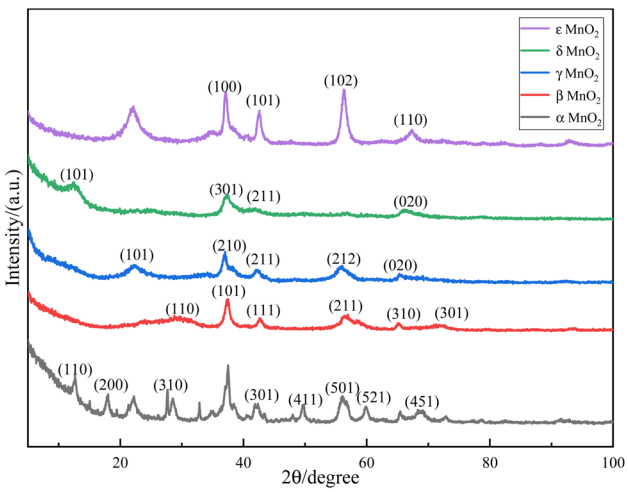

Fig. 1 XRD patterns of the five crystal forms of manganese dioxide.

forms is poor, and the appearance of impurity peaks is due to the presence of a small amount of other crystal forms in the formation process.

The size of the hydrated sodium ion in sodium sulfate solution is 3.6 Å. If bulk intercalation occurs, the manganese dioxide crystal needs sufficient space. The crystal structure of α-

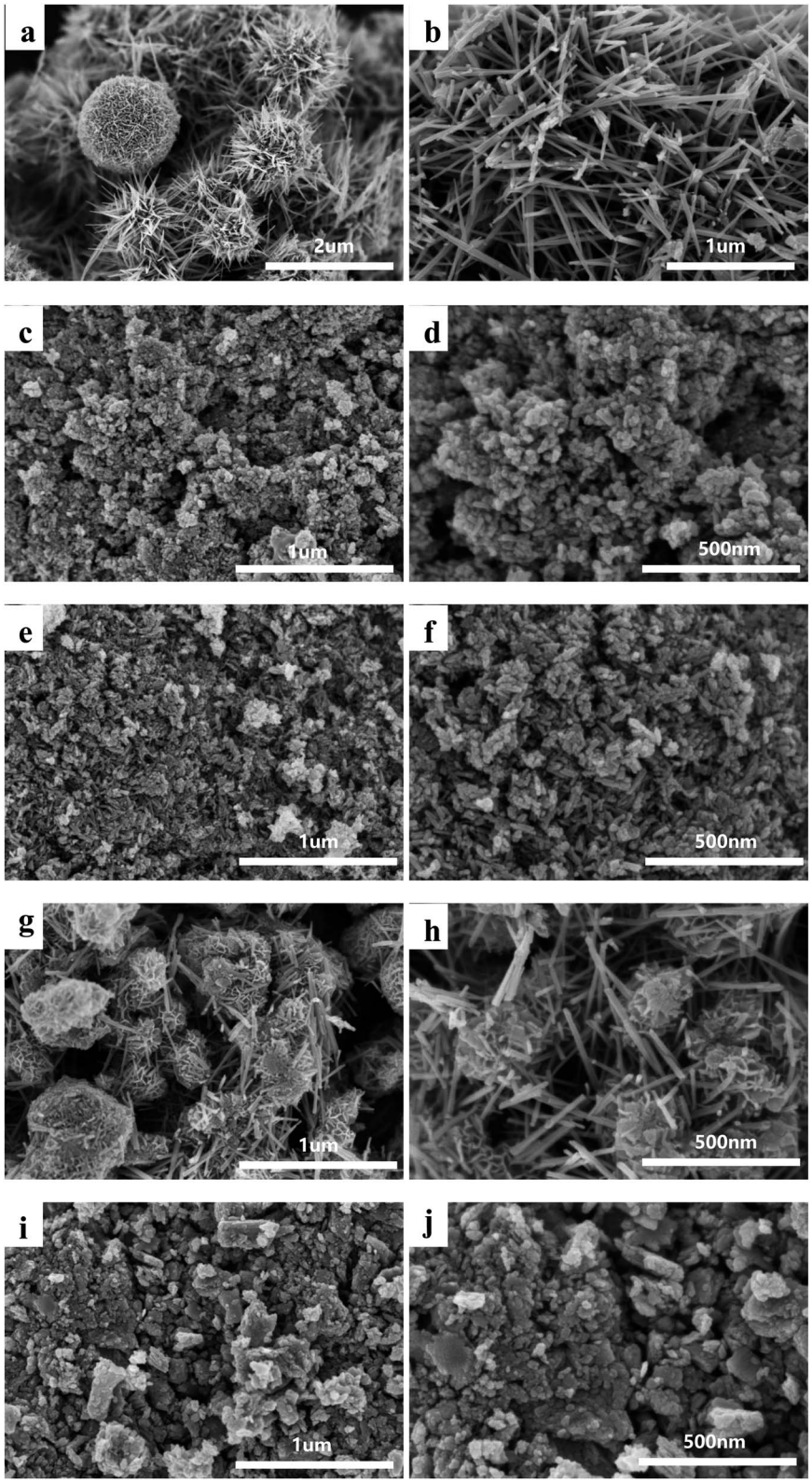

Fig. 2 SEM images of the different crystal forms of manganese dioxide: (a and b) α-MnO_2, (c and d) β-MnO_2, (e and f) γ-MnO_2, (g and h) δ-MnO_2, (i and j) ε-MnO_2.

MnO_2 is mainly a 2 × 2 tunnel composed of double chains, and the tunnel structure size is 4.6 Å, which is very convenient for the insertion–deinsertion of alkali metal ions and is very beneficial for charge storage. β-MnO_2 is a 1 × 1 tunnel composed of single chains. Compared with the former, the tunnel size of the crystal structure is only 1.89 Å, so this tunnel structure cannot accommodate metal cations, so this structure MnO_2 has relatively poor electrochemical performance. γ-MnO_2 contains 1 × 1 and 2 × 1 tunnel structures with sizes of 2.3 × 2.3 Å and 4.6 × 2.3 Å. It is often a symbiont composed of orthorhombic manganese ore and pyrolusite, and cation intercalation is limited by certain size. δ-MnO_2 is a typical layered structure, and its interlayer spacing is generally about 7 Å. The interlayer of such MnO_2 usually contains a large amount of crystal water and metal ions such as Na^+ or K^+, and their presence in the interlayer can make the overall structure more stable. Its wider interlayer spacing is very favorable for the diffusion of hydrated metal cations with a larger radius. The manganese lattice points are highly disordered, the tunnel shape is irregular, and the cation diffusion is difficult in ε-MnO_2. Therefore, when the MnO_2 pseudocapacitor part undergoes a redox reaction in the form of cation intercalation, α-MnO_2 and δ-MnO_2 have the best electrochemical performance, followed by γ-MnO_2, while β-MnO_2 and ε-MnO_2 have poor performance.

It can be seen from Fig. 2 that the α-MnO_2 prepared is generally nano-tubular with irregular morphology. It is composed of interlaced nanospheres and nanorods, which are reunited without an obvious boundary. And the diameter of the nanotubes is about 19 nm. The crystal morphology of β-MnO_2 is nano-balls, accompanied by some nano-rods, the size is uneven, and the edges are blurred. The diameter of nano-balls is about 11 nm. The γ-MnO_2 is regular nanorods with a small amount of agglomeration. The nanorods are long, with an average length of about 40 nm and a diameter of about 9 nm. δ-MnO_2 consists of 'flower-like spheres' and nanotubes with a relatively large diameter; the spherical diameter is about 230 nm, and the nanotube diameter is about 12 nm. ε-MnO_2 consists of irregular nanospheres with different sizes. The nanorods and nanospheres have smaller diameters, which can increase the number of redox reaction active sites and improve the capacity. It can also reduce the diffusion path, and is conducive to high rate charge and discharge. In addition, MnO_2 nanotubes and nanorods have a cavity structure that can withstand volume changes caused by ion movement during cycling, and they can maintain the stability of active substance structure and extend the service life of electrodes. Therefore, γ-MnO_2 can provide relatively more active sites, followed by β-MnO_2, while α-MnO_2 can provide fewer active sites. δ-MnO_2 is different from the other four. In addition to the nanotubes providing more active sites, the flower-like folds on the flower-like spherical surface can provide a larger specific surface area, which is conducive to the occurrence of surface redox reactions. Through morphological analysis, δ-MnO_2 and γ-MnO_2 should have better electrochemical performance, and the other three crystal forms have relatively poor electrochemical performance.

3.2 Analysis of specific surface area and pore structure

Fig. 3 shows the isothermal adsorption and desorption curves of the five crystal forms of manganese dioxide. According to the classification of hysteresis loops by the International Union of Pure and Applied Chemistry in 2015, it can be seen that the hysteresis loops of α-MnO_2, β-MnO_2 and γ-MnO_2 belong to H2(b) type, they are ink bottle-shaped mesoporous with a relatively wide pore 'neck'. Table 1 shows that the average pore diameters of α-MnO_2, β-MnO_2 and γ-MnO_2 are 9.23881, 14.95942 and 14.13070 nm, respectively. δ-MnO_2 is an aggregate with layered structure which has an H3 type hysteresis loop, the pore structure is composed of mesopores or macropores producing slits, the average pore size is 9.20520 nm. ε-MnO_2 has an H4 type hysteresis loop, containing narrow pores, which are mostly micropores, and the average pore size is 5.05786 nm; it has the smallest average pore diameter among the five crystal forms. The total pore volume of γ-MnO_2 is the largest and it is 0.54 $cm^3\ g^{-1}$, about 1.5 times that of δ-MnO_2, 3–4 times that of β-MnO_2, and the total pore volume of ε-MnO_2 is the smallest.

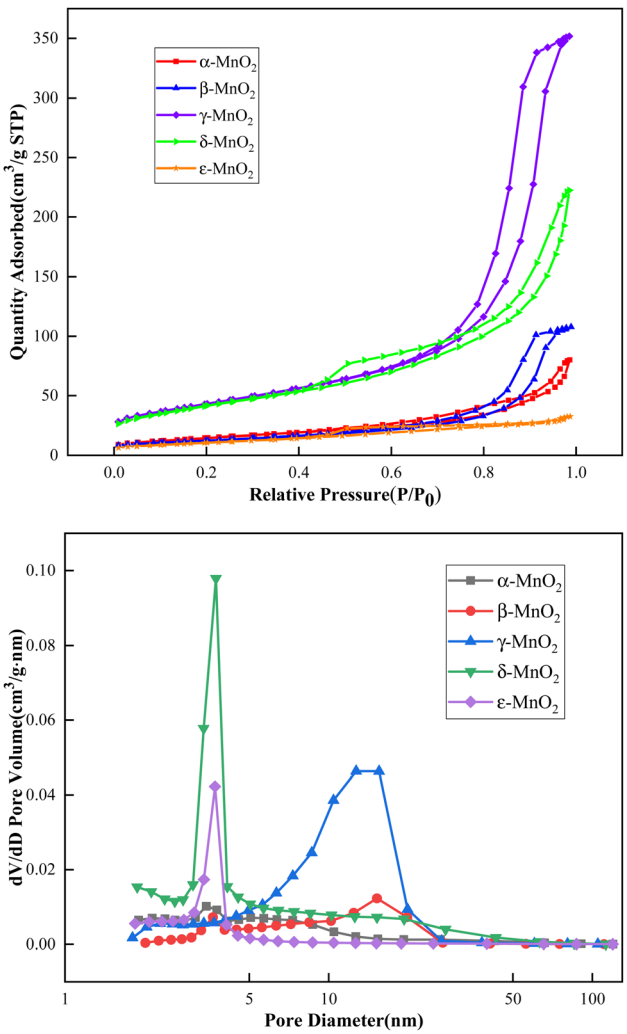

Fig. 3 Isothermal adsorption desorption and pore size distribution curves of different crystal forms of manganese dioxide.

Table 1 Specific surface area, pore volume, pore size and particle size of different crystal forms of manganese dioxide

Crystal form	α-MnO_2	β-MnO_2	γ-MnO_2	δ-MnO_2	ε-MnO_2
BET specific surface area (m^2 g^{-1})	52.41	44.25	153.96	148.59	39.12
Total pore volume (cm^3 g^{-1})	0.12	0.17	0.54	0.34	0.05
Average pore size (nm)	9.24	14.96	14.13	9.21	5.06
Average particle size (nm)	114.49	135.58	38.97	40.38	153.37

The larger the pore size is, the faster the ion diffusion into and out of the hole is, and the more the amount of entry is. The larger the pore volume is, the more ions can be contained, the larger the inner wall area of the pore is, and the more the number of active sites of the ion contact is. Large pore volume and aperture can provide high capacity and high magnification performance. The pore sizes of β-MnO_2 and γ-MnO_2 are larger, and the ion diffusion rate in and out of the pores is faster than that of the other three crystal forms. The large pore volumes of γ-MnO_2 and δ-MnO_2 contribute to their capacity.

The specific surface area of the five crystal forms of manganese dioxide was calculated by the BET method. From 39.12 m^2 g^{-1} for ε-MnO_2 to 153.96 m^2 g^{-1} for γ-MnO_2, the order from small to large is ε-MnO_2 < β-MnO_2 < α-MnO_2 < δ-MnO_2 < γ-MnO_2, and the specific surface area measured by mesopores also increases in the above order. The specific surface area of δ-MnO_2 and γ-MnO_2 is much larger than that of the other three crystal forms. The large specific surface area provides a large number of active sites, and the ions in the electrolyte contact the electrode materials more fully, which is conducive to the rapid surface redox reaction and even the occurrence of in–out phase reaction. Therefore, the large specific surface area will make δ-MnO_2 and γ-MnO_2 have higher capacity than the other three crystal forms. The average particle size of γ-MnO_2 and δ-MnO_2 is much smaller than that of the other three crystal forms of MnO_2, and is about 40 nm. The smaller particle size increases the probability of ions contacting manganese dioxide, shortens the diffusion distance of ions in the bulk phase, and makes full use of the ion transport channels in the bulk phase.

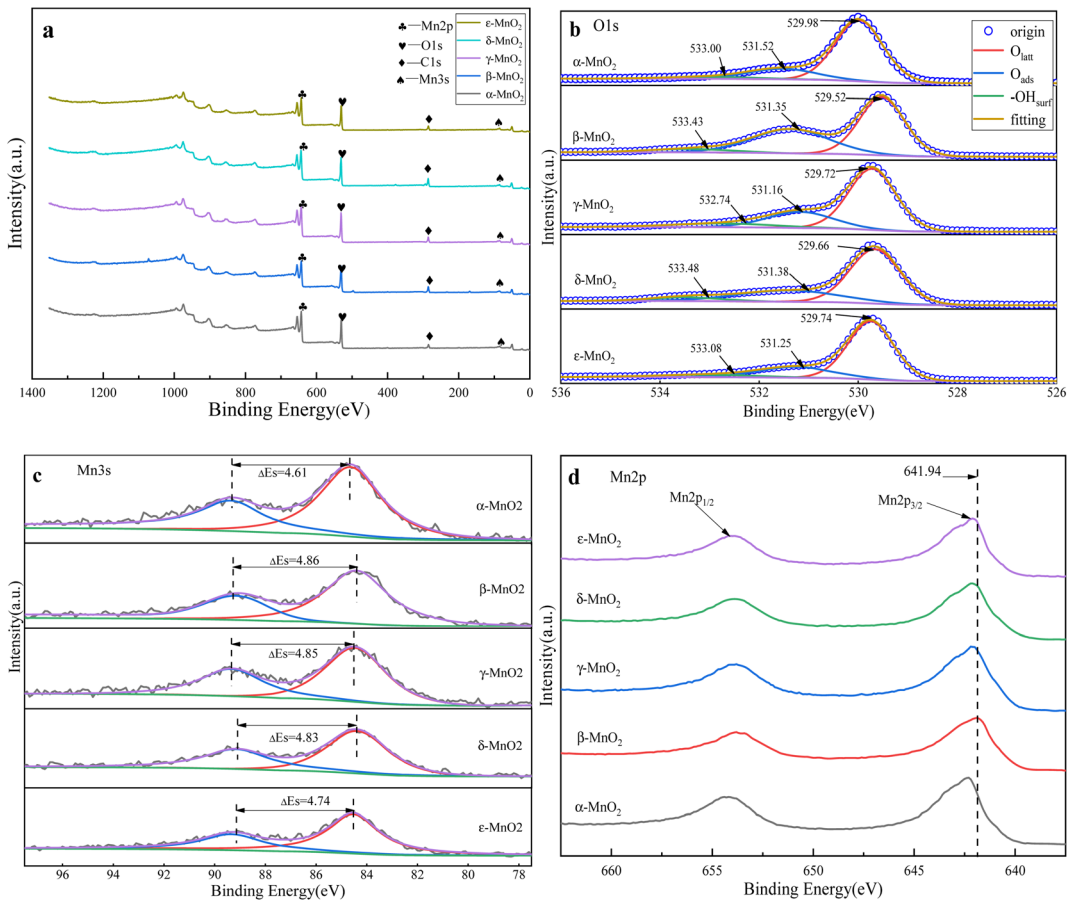

Fig. 4 XPS spectra of different crystal forms of manganese dioxide: (a) main spectrum, (b) O 1s spectrum, (c) Mn 3s spectrum, (d) Mn 2p spectrum.

Table 2 Surface bound oxygen, adsorbed oxygen, hydroxyl and fitting data of the surface average valence

Crystal form	Surface bond oxygen ratio (%)	Adsorbed oxygen ratio (%)	Hydroxyl ratio (%)	ΔE_s/eV	AOS = 8.956 − 1.126ΔE_s
α-MnO_2	76.45	18.78	4.77	4.61	3.77
β-MnO_2	55.24	38.90	5.87	4.86	3.48
γ-MnO_2	66.75	24.47	8.78	4.85	3.49
δ-MnO_2	65.77	27.84	6.39	4.83	3.52
ε-MnO_2	71.88	21.29	6.83	4.74	3.62

3.3 Surface structure characterization

From Fig. 4, it can be seen that the XPS spectra of the five crystal forms of manganese dioxide, and the chemical properties of surface oxygen and manganese elements of MnO_2 samples are obtained by analysis. From the O 1s spectrum, the binding energy near 529 eV corresponds to the lattice oxygen O_{latt} on the surface of manganese dioxide, that at 531 eV corresponds to the adsorbed oxygen O_{ads}, and the binding energy near 533 eV corresponds to the surface hydroxyl group. The surface adsorbed oxygen, lattice oxygen and hydroxyl ratio of each MnO_2 sample was calculated by peak fitting, and is shown in Table 2. From Table 2, the proportion of adsorbed oxygen on the surface of β-MnO_2 is 38.9%, which is the highest among the five MnO_2 samples, followed by δ-MnO_2 (27.84%) and γ-MnO_2 (24.47%), the surface adsorbed oxygen of ε-MnO_2 was lower (21.29%), the surface adsorbed oxygen of α-MnO_2 is the lowest at only 18.78%. The surface hydroxyl content of γ-MnO_2 is the highest, and the hydroxyl content of δ-MnO_2 is in the middle. The oxygen content shown by the surface adsorbed oxygen and surface hydroxyl refers to the surface oxygen vacancy. The surface oxygen vacancies will form a local electric field around themselves, which is conducive to charge transfer in the electrochemical process. The higher the oxygen vacancy concentration is, the higher the capacitance and charge transfer rate are.[79] β-MnO_2 has the most abundant oxygen vacancy concentration, followed by γ-MnO_2 and δ-MnO_2, which is more favorable for charge transfer than the other two crystal forms.

The splitting peak energy level spacing ΔE_s was calculated in combination with the Mn 3s spectrum. The average valence state of Mn element in the five crystal forms of manganese dioxide was obtained according to the formula AOS = 8.956 − 1.126ΔE_s,[80] and the results are shown in Table 1. From Table 1, the average valence state of Mn in α-MnO_2 is the highest, being 3.77, while the valence states of Mn in β-MnO_2, γ-MnO_2 and δ-MnO_2 are 3.48, 3.49 and 3.52, respectively. The results show that the number of Mn^{3+} ions on the surface of β-MnO_2, γ-MnO_2 and δ-MnO_2 is more than that of the other two crystal forms. The change of valence state of manganese can be judged by the shift of the peak position in the Mn $2p_{3/2}$ spectrum. When the peak shifts to the direction of high binding energy, the valence state of the element increases, otherwise, the valence state decreases. From Fig. 4(d), the peaks of β-MnO_2, γ-MnO_2 and δ-MnO_2 shift to lower binding energy, which is consistent with the calculation result of the Mn valence state in the Mn 3s spectrum. The lower average valence state of Mn further indicates the existence of abundant oxygen vacancies. Thus, the lower average valence state is conducive to charge transfer, helping to obtain higher specific capacitance.

The characteristics of surface functional groups from different crystal forms of MnO_2 were analyzed by FT-IR, and the results are shown in Fig. 5. The absorption peak at 500–600 cm^{-1} was the characteristic absorption peak of the Mn–O bond and the vibration peak of impurities contained in manganese dioxide, indicating that they were all manganese dioxide. The medium and low intensity absorption peaks near 1380, 1100 and 1050 cm^{-1} were C–O stretching vibration peaks. CO_2 in the air was adsorbed on the surface of porous manganese dioxide and formed CO_3^{2-} in the pore structure, resulting in the appearance of stretching vibration peaks. The absorption peak at 1635 cm^{-1} is the hydroxyl bending vibration peak. The absorption peak near 3425 cm^{-1} is the absorption peak of hydroxyl stretching vibration. Hydroxyl mainly comes from microporous water with strong binding force and interlayer water inside manganese dioxide crystal, also known as bound water. These hydroxyl groups have a positive effect on improving the activity of manganese dioxide, because bound water and microporous water facilitate ion migration in the electrolyte. δ-MnO_2 has a wider and stronger hydroxyl stretching vibration peak, which shows that its hydroxyl is the most abundant and it contributes to its stronger electrochemical activity.

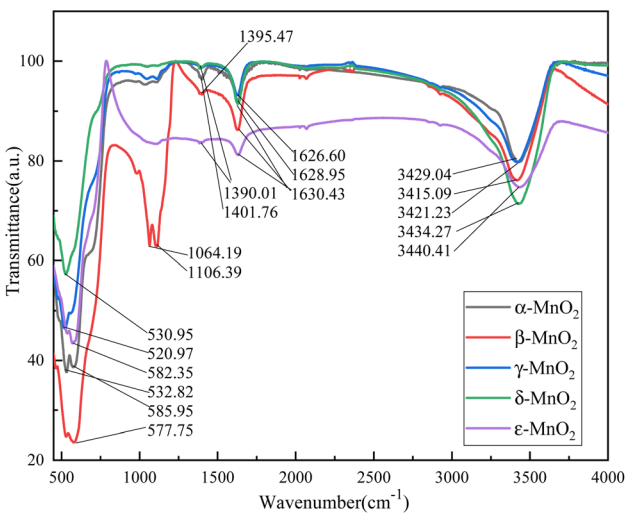

Fig. 5 FTIR spectra of different crystal forms of manganese dioxide.

4 Electrochemical performance analysis

4.1 Capability calculation

The CV curves of the five crystal forms of manganese dioxide were tested in a three-electrode system using an electrochemical workstation. The voltage window was 0–1 V and the scanning speed was 1 mV s^{-1}, and the results are shown in Fig. 6.

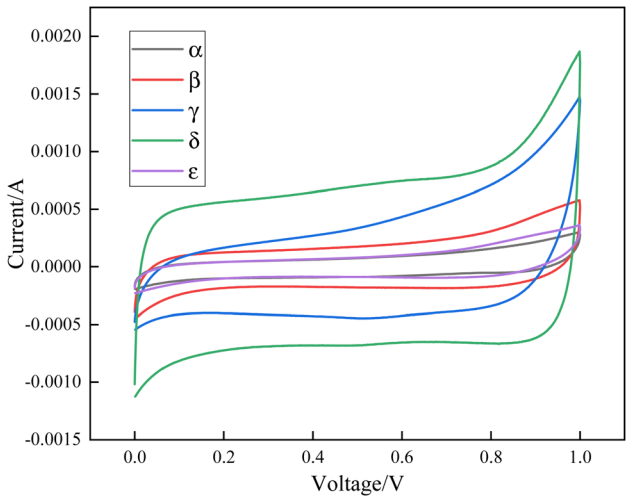

Fig. 6 CV curves of manganese dioxide.

The CV curves of the five crystal forms of manganese dioxide were measured, and the area in the curve was calculated. The mass specific capacitance was calculated using Formula (1). δ-MnO_2 has the highest specific capacitance and its specific capacitance is 73.25 F g^{-1}, γ-MnO_2 takes the second place and its specific capacitance is 66.15 F g^{-1}, that of β-MnO_2 is 31.87 F g^{-1}, and that of α-MnO_2 and ε-MnO_2 is only 15.76 and 16.60 F g^{-1}, respectively. The specific capacities of δ-MnO_2 and γ-MnO_2 are significantly higher than those of the other three crystal forms. δ-MnO_2 has a layered crystal structure with 7 Å interlayer spacing, a flower-like shape and a large specific surface area. At the same time it has interlayer bound water and the surface oxygen vacancy concentration is high. These physical and chemical properties make δ-MnO_2 have high specific capacitance. The γ-MnO_2 crystal tunnel structure has a negative effect on ion migration, but its better morphology, larger specific surface area and higher oxygen vacancy concentration are beneficial to electrochemical performance. Although the tunnel size of β-MnO_2 is small, its specific capacitance is larger than that of α-MnO_2 due to the abundant oxygen vacancies and larger pore volume. α-MnO_2 has the largest tunnel size, but because of its less oxygen vacancies, relatively small specific surface area, pore diameter and pore volume, as well as larger nanotube size, its specific capacitance is lower. The disordered

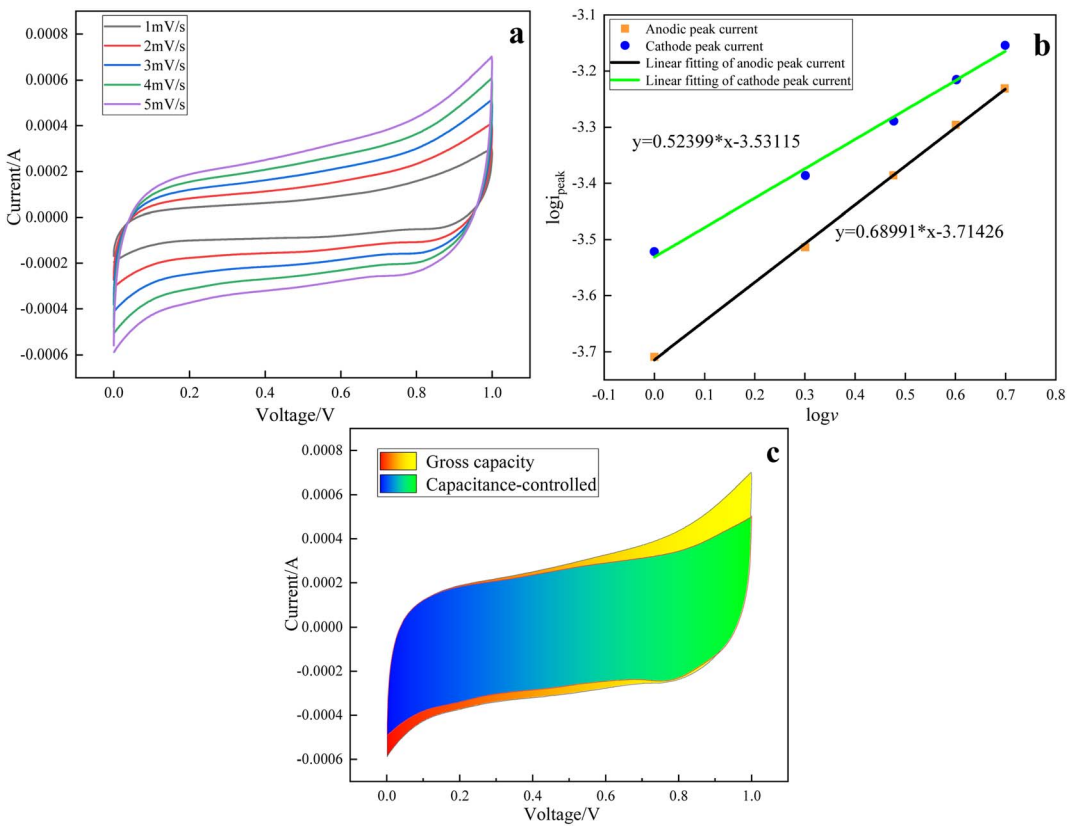

Fig. 7 Analysis diagram of the α-MnO_2 electrode reaction process: (a) CV curves at different scanning speeds, (b) calculation of the *b* value, (c) calculation of the capacitance control area and total area.

crystal structure, smaller specific surface area, pore diameter and pore volume, and fewer oxygen vacancies of MnO_2 will lead to its low capacity.

4.2 Analysis of electrode kinetic process

To the five crystal forms of manganese dioxide, the kinetic analysis of the electrochemical process was carried out in the three-electrode system. The CV curves were recorded at the scan rates of 1 mV s^{-1}, 2 mV s^{-1}, 3 mV s^{-1}, 4 mV s^{-1}, and 5 mV s^{-1}; then the electrode reaction control process was analyzed qualitatively and quantitatively according to the measured CV curve. The analysis calculation process is as follows.

The capacity composition of manganese dioxide pseudocapacitive materials generally consists of two parts. One part is capacitance control, which mainly includes electric double layer and surface redox reaction, and the other part is diffusion control, that is, the electrolyte cation enters the manganese dioxide phase and undergoes intercalation redox reaction in the crystal structure. The redox reaction equations of the two control processes are as follows, $MnO_2 + A^+ + e^- \leftrightarrow MnOOA$, where A can be H, Na and other cations in the electrolyte. Since the time required for the two control processes to occur is different, they can be distinguished using kinetic knowledge.

The CV curves at different scan rates, fitting curves for qualitative analysis of the b-value, capacitance contribution capacity, and specific capacitance contributed by the capacitance process and diffusion process are shown in Fig. 7–11. The kinetics of the electrode in the reaction process can be analyzed qualitatively using $i = av^b$. The dynamic process is controlled by capacitance when $b = 1$. This process occurs faster. The dynamic process is controlled by semi-infinite diffusion when $b = 0.5$. This process takes a long time and the process is slow. The b value corresponding to the anode and cathode can be obtained by using CV curves, peak current and the linear graph fitted by sweep speed. Since the scan is completed in the anode direction, there is a lag when the cathode is scanned in reverse. The b value is obtained with the positive linear fitting slope. It can be seen that the b value of the five crystal forms is between 0.5 and 1, so there is both the capacitance part and bulk phase diffusion part.

In order to further explain the proportion of the capacitance part and the diffusion part in the five crystal forms, a quantitative analysis is carried out. The proportion is calculated by using the formula $i(V) = k_1v + k_2v^{0.5}$, where k_1v is the capacitance contribution, which mainly includes the double electric layer, that is, the physical capacitance and the surface redox reaction contribution. $k_2v^{0.5}$ is the diffusion contribution; it refers to the

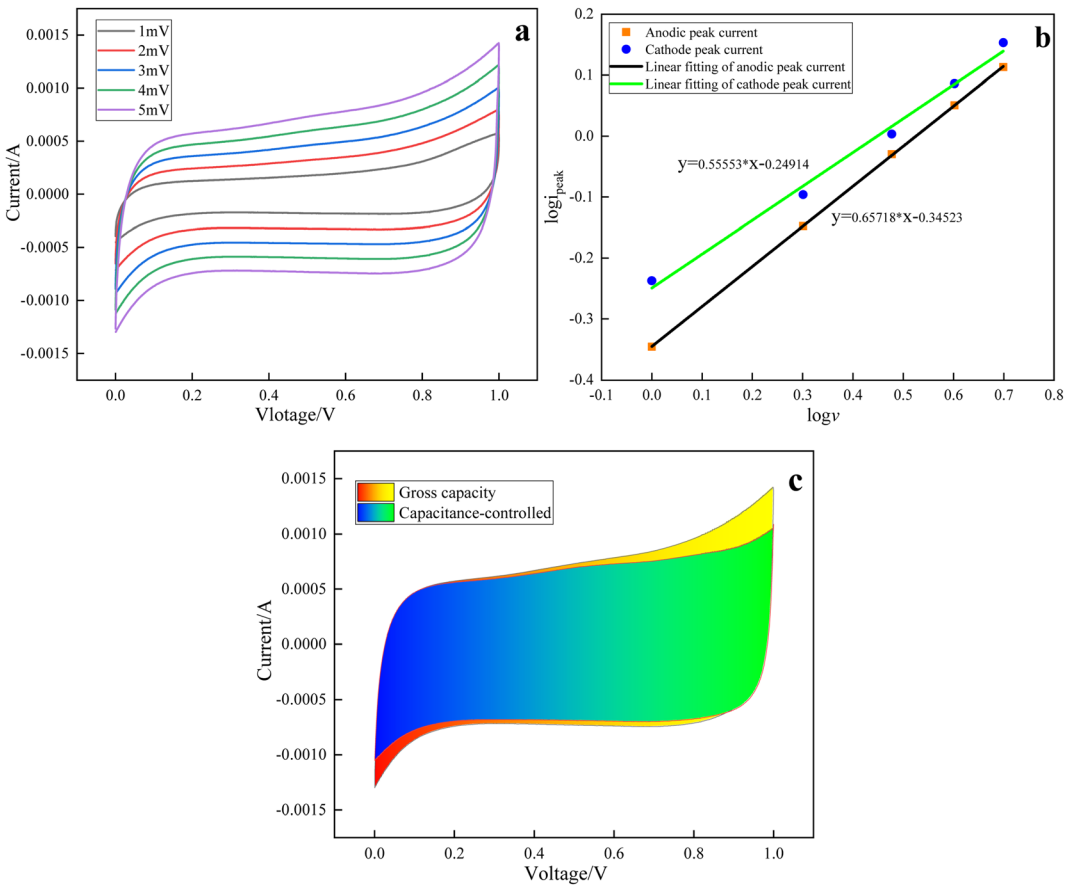

Fig. 8 Analysis diagram of the β-MnO_2 electrode reaction process: (a) CV curves at different scanning speeds, (b) calculation of the b value, (c) calculation of the capacitance control area and total area.

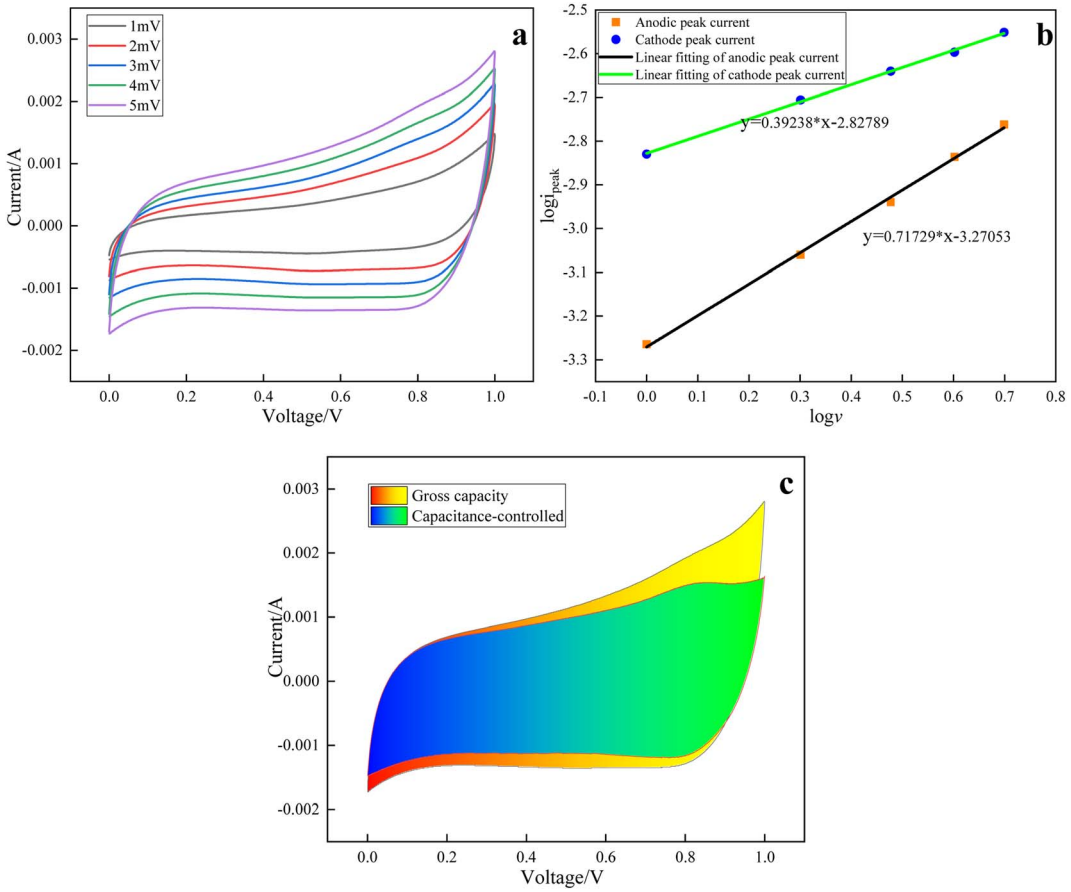

Fig. 9 Analysis diagram of the γ-MnO_2 electrode reaction process: (a) CV curves at different scanning speeds, (b) calculation of the *b* value, (c) calculation of the capacitance control area and total area.

capacitance generated by the redox reaction in the bulk phase of the electrode material. The proportion of capacitance parts of different crystal forms is shown in Table 3 at the scanning speeds of 1–5 mV s^{-1}. These data show a unified rule: with the increase of scanning speed, the proportion of capacitance gradually increases, and the diffusion control part gradually decreases. This is because the time required for the two processes to occur is different. As the scanning speed becomes faster, the capacitance control part can still occurs quickly, while the time required for the diffusion control part to occur is insufficient. Too fast scanning speed prevents ions from entering the bulk phase for the redox reaction. In other words, higher scanning speed reduces the redox possibility of ions entering the bulk phase, resulting in a decrease in the contribution of the diffusion part.

With reference to the method in the literature,[81] when the scanning speed is 1 mV s^{-1}, the composition of specific capacitance contribution is analyzed according to the electrochemical test results of the five crystal forms of manganese dioxide. The results are shown in part (c) of Figure7–11. Due to the polarization of the electrode material, the capacitance ratio fitting area exceeds the total capacity area, but does not affect the analysis results. The analysis process of the mechanism influencing the physical and chemical properties and capacity composition of different crystal forms of manganese dioxide is as follows: α-MnO_2 and ε-MnO_2 have poor specific capacity, and the capacitance contribution of the double electric layer and the diffusion contribution of intercalation redox are very low. Although α-MnO_2 has a large tunnel size for cation insertion, it has a small specific surface area and pore volume, large particle size and low oxygen vacancy concentration. So the number of surface active sites was less, ion transfer is slow, surface redox reaction is less and the bulk diffusion contribution is less. In addition to the above shortcomings, the crystal structure of ε-MnO_2 hinders the occurrence of bulk diffusion redox reaction. These properties result in poor conductivity and low capacity of these two crystal forms. MnO_2 has a high oxygen vacancy on its surface, which enhances its charge transfer rate, so the capacitance control has a larger capacity. γ-MnO_2 and δ-MnO_2 have a relatively large specific capacity. Comparing their reaction processes, the former has a capacitance control ratio of 52% at low scan rates, and the diffusion-controlled bulk redox reaction also contributes nearly half, while the latter 83.82% of the specific capacitance contribution comes from capacitance control. The reason is that since γ-MnO_2 has a large specific surface area, and larger pore size and pore volume, the most active sites can be provided. At the same time, larger concentration of oxygen

Table 3 Comparison of the capacitance contribution ratio and corresponding specific capacitance of varying crystal capacitance control and diffusion control at different scan rates

Different sweep speeds		1 mV s^{-1}		2 mV s^{-1}		3 mV s^{-1}		4 mV s^{-1}		5 mV s^{-1}	
Different crystals		Contribution of capacitance	Diffusion contribution	Contribution of capacitance	Diffusion contribution	Contribution of capacitance	Diffusion contribution	Contribution of capacitance	Diffusion contribution	Contribution of capacitance	Diffusion contribution
α-MnO_2	Proportion (%)	60.63	39.37	71.89	28.11	78.83	21.17	84.34	15.66	88.20	11.80
	Specific capacity (F g^{-1})	9.55	6.14	9.55	3.74	9.55	2.57	9.56	1.77	9.55	1.28
β-MnO_2	Proportion (%)	69.00	31.00	79.47	20.53	85.21	14.79	88.82	11.18	91.64	8.36
	Specific capacity (F g^{-1})	21.99	9.88	21.99	5.68	21.99	3.82	21.99	2.77	21.98	2.01
γ-MnO_2	Proportion (%)	52.04	47.96	62.60	37.40	72.37	27.63	78.65	21.35	83.67	16.33
	Specific capacity (F g^{-1})	34.42	31.73	34.42	20.57	34.42	13.14	34.42	9.34	34.42	6.72
δ-MnO_2	Proportion (%)	83.82	16.18	89.02	10.98	92.37	7.63	94.75	5.25	96.05	3.95
	Specific capacity (F g^{-1})	61.40	11.85	61.39	7.57	61.38	5.07	61.39	3.40	61.40	2.52
ε-MnO_2	Proportion (%)	56.32	43.68	67.33	32.67	74.54	25.46	81.88	18.12	85.94	14.06
	Specific capacity (F g^{-1})	9.35	7.25	9.35	4.54	9.08	3.10	9.35	2.07	9.35	1.53

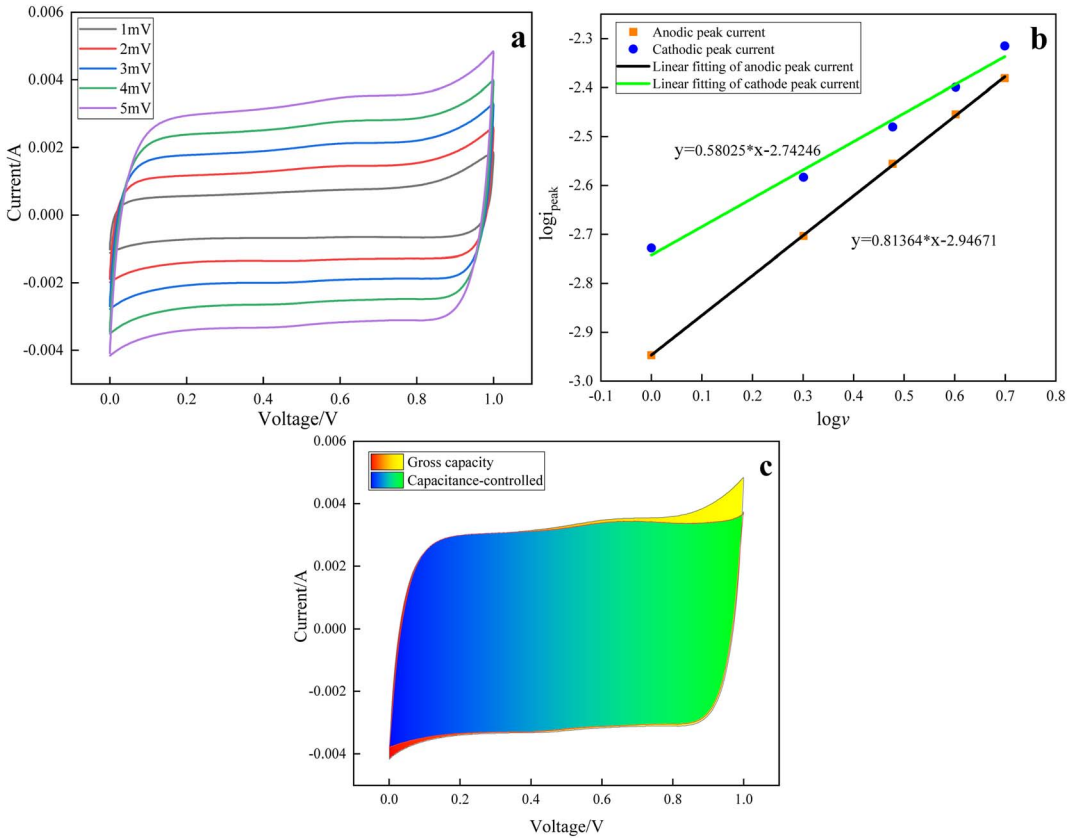

Fig. 10 Analysis diagram of the δ-MnO_2 electrode reaction process: (a) CV curves at different scanning speeds, (b) calculation of the *b* value, (c) calculation of the capacitance control area and total area.

vacancies is conducive to ion transfer. The greater contribution of the diffusion part indicates the occurrence of intercalation. The rod shape, good pore structure, large pore size, large pore volume, small particle size and other characteristics make γ-MnO_2 have more active sites, increasing the possibility of ion intercalation, in which a small amount of sodium ions and hydrogen ions participate in the intercalation. Although δ-MnO_2 has a large crystalline layered structure, because the main contribution of specific surface area comes from the flower ball shape and surface folds, ion diffusion only occurs quickly on the surface, a small amount enters the fold body phase, and the probability of entering the ball under the fold is low, resulting in less diffusion into the body phase. It can be seen from the above analysis that the electrode reactions of α-MnO_2, β-MnO_2, δ-MnO_2, and ε-MnO_2 are mainly controlled by capacitance. Their surfaces can undergo rapid oxidation–reduction reaction, so they have typical capacitive material characteristics, and δ-MnO_2 has the best performance. However, the capacity contribution of γ-MnO_2 intercalation redox reaction is close to that of capacitance, which has certain battery material characteristics.

4.3 Impedance test and fitting

The EIS curves of the five crystal forms of MnO_2 are shown in Fig. 12.

The EIS curves of five kinds of manganese dioxide were obtained by an AC impedance test. The impedance circuit model obtained by ZView fitting is shown in Fig. 12. The solution resistance of these manganese dioxide in sodium sulfate electrolyte was between 3 and 4 Ω basically, because the solution resistance was not much different at the same concentration of sodium sulfate solution. There is only one circular arc in the high frequency and medium frequency regions. This is because the diffusion and migration of sodium ions through the SEI film on the surface of the active material particles and the charge transport inside the active material particles are a couple of coupled processes, and the interface resistance and charge transfer resistance overlap. The interface resistance and charge transfer resistance overlap in the high frequency and intermediate frequency region. The impedance sequence of manganese dioxide is δ < α < β < ε < γ in the high frequency region and the intermediate frequency region, and the impedance of ε-MnO_2 and γ-MnO_2 is much larger than that of the other three crystal forms. The order of diffusion resistance of electrolyte ions in the bulk phase at low frequency is δ < β < α < ε < γ. The above results show that δ-MnO_2 has the smallest impedance among the five crystal forms, which is more conducive to the surface oxidation and intercalation redox reaction of electrolyte ions, so it can obtain the highest specific capacitance among the five crystal forms. γ-MnO_2 has a large charge transfer resistance and bulk

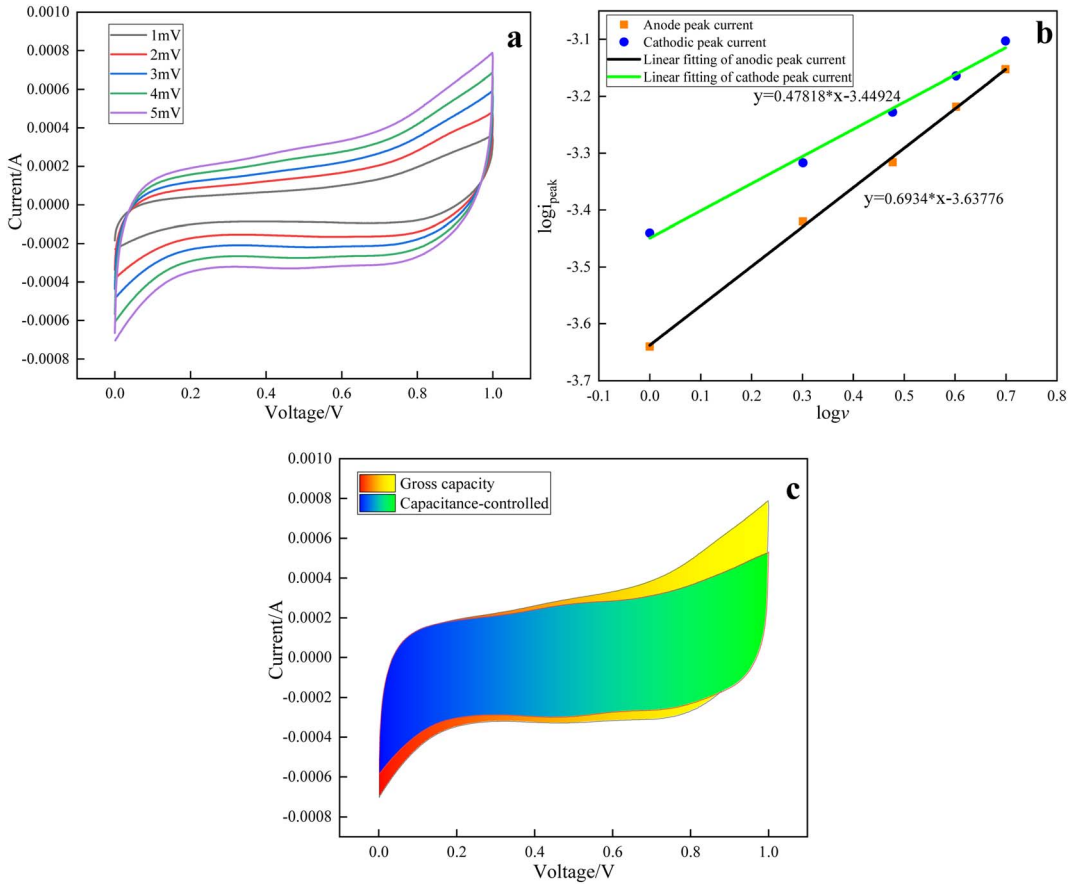

Fig. 11 Analysis diagram of the ε-MnO_2 electrode reaction process: (a) CV curves at different scanning speeds, (b) calculation of the *b* value, (c) calculation of the capacitance control area and total area.

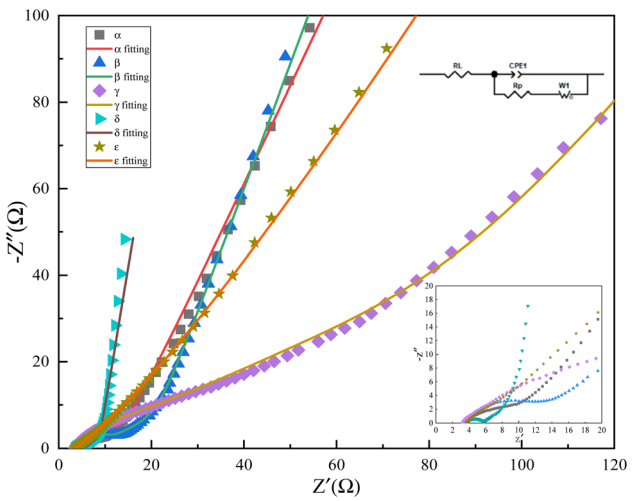

Fig. 12 AC impedance curves of the five crystal forms of manganese dioxide.

diffusion resistance. Even so, it has a higher specific capacitance than the other three crystal forms. If the conductivity can be improved, its specific capacitance will have greater potential for improvement.

5 Constant current charge and discharge performance comparison

The charge–discharge cycle of the electrode sheets prepared by five crystal forms of MnO_2 was carried out on the Xinwei charge–discharge equipment. The experimental conditions are as follows: the electrolyte of the three-electrode system was 1 mol L^{-1} Na_2SO_4, the current density was 0.1 A g^{-1}, and 100 constant current charge–discharge cycles. The specific capacitance is shown in Fig. 13. The lithium manganate prepared from the five crystal forms of MnO_2 is used as cathode to make the lithium battery, with 200 constant current charge and discharge cycles under 1C, and the specific capacity is shown in Fig. 14.

From Fig. 13, it can be seen that the specific capacitance of the electrode materials prepared from the five crystal forms is obtained by constant current charging and discharging in the three-electrode system, and δ-MnO_2 and γ-MnO_2 still have higher specific capacitance. Although the charge specific capacitance of γ-MnO_2 is higher than that of δ-MnO_2, its discharge specific capacitance is lower than that of δ-MnO_2, and the difference between charge and discharge specific capacitance is large. The specific capacitance of δ-MnO_2 cyclic charging and discharging is stable, and the capacity loss is

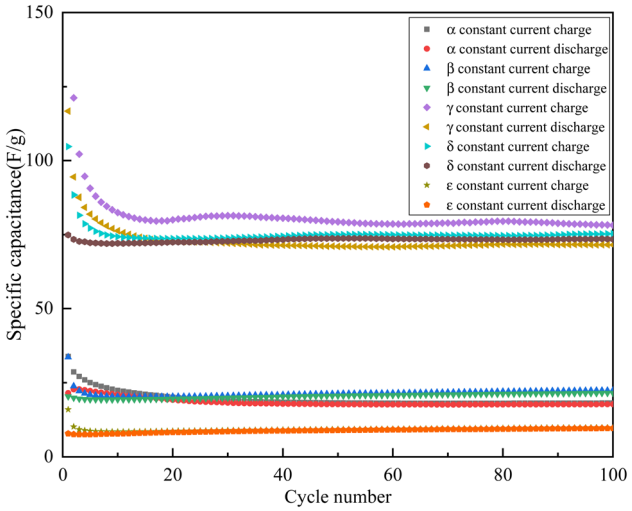

Fig. 13 Long charge–discharge cycles of electrode materials made of the five crystal forms of MnO_2.

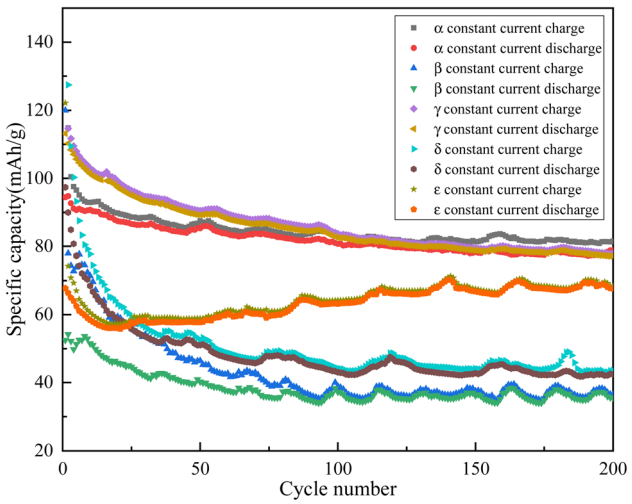

Fig. 14 Long charge–discharge cycles of lithium manganate synthesized from the five crystal forms of manganese dioxide.

small, which is more useful for capacitor materials. From Fig. 14, the specific capacity order of the first cycle is γ-MnO_2 > δ-MnO_2 > α-MnO_2 > ε-MnO_2 > β-MnO_2. The discharge specific capacities of α-MnO_2 and γ-MnO_2 are 78.83 mA h g^{-1} and 77.26 mA h g^{-1} respectively after 200 cycles. The specific capacity retention rate of lithium manganate synthesized by α-MnO_2 and ε-MnO_2 is about 83% after circulation, while that of γ-MnO_2 and β-MnO_2 is about 68%, and that of δ-MnO_2 is the lowest, only 43.59%. It can be seen that γ-MnO_2 has more advantages than δ-MnO_2 as a battery material.

6 Conclusion

Five crystal forms of manganese dioxide, α, β, γ, δ, and ε, were prepared by a liquid phase method. Their phase, morphology, specific surface area, surface structure and specific capacitance were characterized. Among them, δ-MnO_2 has the highest specific capacitance and it is 73.25 F g^{-1}, because it has layered crystals of sufficient size, flower-like spherical shape, large specific surface area, abundant oxygen vacancies, and more interlayer bound water than other crystal forms. The specific capacitance of γ-MnO_2 is only 66.15 F g^{-1}. Its crystal structure is not conducive to ion intercalation, but its specific surface area is larger than that of other crystal forms, and it has larger pore volume, sufficient oxygen vacancies, and smaller particle size. These advantages provide higher specific capacitance. β-MnO_2 has a poor crystal structure and a small specific surface area, but because the concentration of surface oxygen vacancies is the highest among the five crystal forms, its specific capacity ranks third. The specific capacitance of α-MnO_2 and ε-MnO_2 is relatively small. The crystal structure of α-MnO_2 is large, which is conducive to ion penetration, but the smaller specific surface area and lower surface oxygen vacancies make its electrochemical performance poor. In addition to the above shortcomings of α-MnO_2, the unique reason is the disordered crystal structure of ε-MnO_2. Therefore, compared with the other three crystal forms, the two crystal forms of δ and γ manganese dioxide prepared by liquid phase synthesis have relatively good electrochemical performance.

The contribution ratio of capacitance control and bulk diffusion control to capacity can be calculated using the kinetic formula and CV curve. The four crystal forms of α, β, δ and ε are dominated by the contribution of capacitance. Most of the capacitance of β-MnO_2 contributes to the specific capacitance, which is sufficient to show that it has rich structural oxygen vacancies, while the capacitance contribution and diffusion contribution of α-MnO_2 and ε-MnO_2 are very low, indicating that their ion intercalation and surface redox reactions occur less. The high capacitance contribution of δ-MnO_2 indicates that it can be used as a fast charge and discharge capacitor material. The capacitance contribution and diffusion contribution of γ-MnO_2 are almost equal at low scanning rate, which is caused by ion bulk diffusion, indicating a better battery material performance. The EIS test of the five crystal forms of MnO_2 shows that δ-MnO_2 has the smallest charge transfer impedance and diffusion impedance, while the two kinds of impedance of γ-MnO_2 are the largest. If the impedance is reduced, its capacity will be further improved and the potential is huge. The five crystal forms were tested by constant current charge and discharge in an aqueous three-electrode and synthetic battery cathode lithium manganate. It was found that δ-MnO_2 had relatively stable and large specific capacitance during constant current charge and discharge of pseudocapacitance, which was more suitable for rapid charge and discharge. The specific capacity of γ-MnO_2 is large and relatively stable during constant current charge and discharge, which is more suitable for the synthesis of lithium manganate as a battery cathode material.

In this study, five crystal forms of manganese dioxide were synthesized by a liquid phase method and their properties were characterized. The relationship between physical and chemical properties and electrochemical properties was studied. The performance of different crystal forms of manganese dioxide for

capacitor materials and battery materials was explored. It is concluded that liquid phase preparation is more suitable for capacitor and battery materials. Manganese dioxide provides research ideas for industrial replacement of electrolytic production of manganese dioxide.

Conflicts of interest

There are no conflicts to declare.

Acknowledgements

The funding support for this study was obtained from the National Natural Science Foundation of China (51864012), Key projects supported by science and technology in Guizhou Province ([2002]key020), Major special projects in Guizhou Province ([2022]003), Guizhou Provincial Science Cooperation Program ([2016]5302, [2017]5788, [2018]5781, [2019]1411, [2019]2841), and Major special projects in Tongren City, Guizhou Province ([2021]13). The authors sincerely thank the reviewers for their views and suggestions to further improve the quality of the manuscript.

References

1 G. H. Jiang, Q. S. Ouyang, M. Y. Hu, S. Q. Zhang, Q. F. Zhao and C. Wang, Research Progress in Preparation and Application of Manganese Dioxide/Graphene Composites, *Hunan Youse Jinshu*, 2021, **37**(04), 51–55.

2 Y. Zhao, Fabrication and Assembly of Supercapacitor Based on MnO_2 electrode material, Shenyang University of Technology, 2021, DOI: 10.27322/d.cnki.gsgyu.2021.000937.

3 A. Q. Zhang, Preparation of manganese dioxide with optimized electronic structure for supercapacitors, Beijing University of Chemical Technology, 2021, DOI: 10.26939/d.cnki.gbhgu.2021.000777.

4 D. Majumdar, Review on current progress of MnO_2-Based ternary nanocomposites for supercapacitor applications, *ChemElectroChem*, 2020, **8**, 291–336.

5 X. Zhao, Y. Hou, Y. Wang, *et al.*, Prepared MnO_2 with different crystal forms as electrode materials for supercapacitors:experimental research from hydrothermal crystallization process to electrochemical performances, *RSC Adv.*, 2017, **7**, 40286–40294.

6 J. Shin, J. K. Seo, R. Yaylian, *et al.*, A review on mechanistic understanding of MnO_2 in aqueous electrolyte for electrical energy storage systems, *Int. Mater. Rev.*, 2020, **65**, 356–387.

7 B. S. Shen, Preparation of manganese dioxide and its composites and study on the performance of supercapacitor, Beijing University of Chemical Technology, 2021.

8 P. Cui, Research on improving the performance of manganese dioxide supercapacitors based on defect engineering, Lanzhou University, 2021, DOI: 10.27204/d.cnki.glzhu.2021.002061.

9 X. Long, Synthesis and energy storage performance of MnO_2-based self-supported electrodes, Lanzhou University, 2021, DOI: 10.27204/d.cnki.glzhu.2021.000206. in Chinese.

10 C. L. Li, J. F. Yang, J. L. Zhu, L. C. Zhang and X. P. Wang, Structure and properties of $LiMn_2O_4$ synthesized by complex manganese precursor, *Trans. Mater. Heat Treat.*, 2022, **43**(04), 27–33.

11 S. M. Qiu, Y. Y. Huang, W. Hu, M. Cai, X. B. Qin, W. Q. Zou and S. w. Liu, Study on preparation and performance of $LiNi_{0.5}Mn_{1.5}O_4$ high-voltage cathode material, *New Chem. Mater.*, 2021, **49**(03), 108–112.

12 W. Li, *Study on the Preparation and Performance of Cathode Material Lithium Manganese Oxide for Power Lithium Ion Batteries*, University of Science and Technology Beijing, 2017, in Chinese.

13 Q. L. Wei, X. Y. Wang, X. K. Yang, H. B. Shu, B. W. Ju, B. A. Hu and Y. F. Song, Effects of ball milling on the crystal face of spinel $LiMn_2O_4$,*J. Solid State Electrochem.*, 2012, **16**, 3651–3659.

14 C. B. Wei, J. X. Shen, J. Y. Zhang, H. Y. Zhang and C. F. Zhu, Effects of ball milling on the crystal face of spinel $LiMn_2O_4$, *RSC Adv.*, 2014, **4**, 44525–44528.

15 A. Baral, L. Satish, G. Y. Zhang, *et al.*, A review of recent progress on nano mno_2: synthesis, surface modification and applications, *J. Inorg. Organomet. Polym. Mater.*, 2021, **31**(3), 899–922.

16 S. Dawadi, A. Gupta, M. Khatatri, *et al.*, Manganese dioxide nanoparticles: synthesis, application and challenges, *Bull. Mater. Sci.*, 2020, **43**(1), 277.

17 B. B. Ding, P. Zheng, P. Ma, *et al.*, Manganese oxide nanomaterials: synthesis, properties, and theranostic applications [J], *Adv. Mater.*, 2020, **32**(10), e1905823.

18 X. Z. Xie, *Preparation and Properties of Mno_2 Composite Phase Change Materials with Different Crystal Forms and Different Morphologies*, Dalian Jiaotong University, 2019, In Chinese.

19 Z. Han, T. S. Yu, W. T. Liu, M. Zhang, H. X. Jin, H. L. Ge, X. Q. Wang and D. F. Jin, Preparation,characterization and catalytic degradation performance of formaldehyde of different manganese dioxide., *J. China Univ. Metrol.*, 2021, **32**(01), 124–131.

20 N. C. Xu and D. D. Shi, Preparation of manganese dioxide nanomaterials with different crystalline and their adsorption properties to methylene blue, *Inorg. Chem.: Indian J.*, 2021, **53**(03), 44–47.

21 P. Zhao, M. Q. Yao, H. B. Ren, *et al.*, Nanocomposites of hierar-chical ultrathin MnO_2 nanosheets/hollow carbon nanofibers for high-performance asymmetric supercapacitors, *Appl. Surf. Sci.*, 2019, **463**, 931–938.

22 F. F. Wu, X. B. Gao, X. L. Xu, *et al.*, Boosted Zn storage performance of MnO_2 nanosheet-assembled hollow polyhedron grown on carbon cloth via a facile wet-chemical synthesis, *ChemSusChem*, 2020, **13**(6), 1537–1545.

23 C. J. Lu, F. Q. Zhu, J. G. Yin, *et al.*, Synthesis of α-MnO_2 nanowires via facile hydrothermal method and their application in Li-O_2 bat-tery, *J. Inorg. Mater.*, 2018, **33**(9), 1029–1034.

24 K. Zhu, C. Wang, P. H. C. Camargo, *et al.*, Investigating the effect of MnO_2 band gap in hybrid MnO_2-Au materials over

the SPR-mediated activities under visible light, *J. Mater. Chem. A*, 2019, **7**(3), 925–931.

25 D. Y. Liu, L. M. Dong, L. W. Shan, *et al.* Preparation of Fe-MnO_2/RGO electrode and electrochemical properties, *Ferroelectrics*, 2019, **546**(1), 41–47.

26 A. Mathur and A. Halder, One step synthesis of bifunctional iron-doped manganese oxide nanorods for rechargeable zinc-air batteries, *Catal. Sci. Technol.*, 2019, **9**(5), 1245–1254.

27 W. B. Gao, *Studies on Polydopamine-Based and Template-Directed Preparation of Manganese Oxide Nanotube Array and Polydopamine-Based Electrochemical Analysis*, University of Science and Technology Beijing, 2017, in Chinese.

28 N. Y. Zhao, J. P. Bian, X. J. Yang, *et al.* Preparation of La-doped nano MnO_2 by sol-gel method, *New Chem. Mater.*, 2019, **47**(5), 164–171.

29 Z. Li, H. W. Tang and B. N. Wang, Study of adsorption property of nanosized MnO_2/diatomite to phenolic wastewater, *J. Hefei Univ. Technol., Nat. Sci.*, 2016, **39**(5), 695–700.

30 H. T. Wu, Z. Z. Zhang, F. X. Zhang, *et al.* Performance of nano-α-MnO_2 synthesized via low temperature solid-phase method, *Dianchi*, 2015, **45**(3), 157–159.

31 L. Y. Gong, The capacitive behavior of MnO_2 nanorods synthesized by Solid-state reaction and the doping modification of PbO to MnO_2 nanorods, *J. Qingdao Agric. Univ.*, 2011, **28**(2), 157–161.

32 S. M. Xie, Q. Qin, Z. H. Zhang, *et al.* Microwave Synthesis of SnO_2/Activated Carbon Particle Electrode and Degradation of 4-Chlorophenol, *Technol. Water Treat.*, 2021, **47**(02), 32–37.

33 C. Zhou, *Study on Microwave Synthesis of 1D/2D Composite Nanomaterials and Their Synergistic Catalytic Activity*, Shanghai Normal University, 2020, in Chinese.

34 X. L. Chen, Study on the regulation mechanism of manganese oxide prepared by H_2O_2 in-situ oxidation method, Guizhou University, 2021.

35 J. M. Wang, H. Y. Yu and D. Y. Ma, Progress in the Preparation and Application of Nanostructured Manganese Dioxide, *J. Inorg. Mater.*, 2020, **35**(12), 1307–1314.

36 M. D. Li, J. W. Wang, B. B. Gou, D. J. Fu, H. F. Wang and P. Y. Zhao, Relationship between Surface Hydroxyl Complexation and Equi-Acidity Point pH of MnO_2 and Its Adsorption for Co^{2+} and Ni^{2+}, *ACS Omega*, 2022, **7**(11), 9602–9613.

37 B. B. Chen, B. Wu, L. M. Yu and etal, Investigation into the catalytic roles of various oxygen species over different crystal phases of MnO_2 for C_6H_6 and HCHO oxidation, *ACS Catal.*, 2020, **10**(11), 6176–6187.

38 Y. Yamaguchi, R. Aono, E. Hayashi and etal, Template-Free Synthesis of Mesoporous beta-MnO_2 Nanoparticles: Structure, Formation Mechanism, and Catalytic Properties, *ACS Appl. Mater. Interfaces*, 2020, **12**(32), 36004–36013.

39 H. Usui, S. Nonaka, S. Suzuki, *et al.*, Photosynthesis-Inspired Electrolyte Additives Enhancing Photoelectrochemical Charge–Discharge Property of TiO_2/MnO_2 Composite Electrode, *ACS Appl. Electron. Mater.*, 2019, **1**(6), 823–827.

40 M. T. Nguyen Digh, C. C. Nguyen, T. L. Truong Vu and etal, Tailoring porous structure, reducibility and Mn^{4+} fraction of ε-MnO_2 microcubes for the complete oxidation of toluene, *Appl. Catal., A*, 2020, 595.

41 S. Yang, H. Yang, J. Yang and etal, Three-dimensional hollow urchin α-MnO_2 for enhanced catalytic activity towards toluene decomposition in post-plasma catalysis, *Chem. Eng. J.*, 2020, **402**, 126154.

42 H. F. Liu, *Synthesis of Manganese Dioxide Catalysts with Different Crystal Types and Their Performances for Catalytic Combustion*, Guangdong University of Technology, 2021, in Chinese.

43 D. Majumdar, Review on current progress of MnO_2-Based ternary nanocomposites for supercapacitor applications, *ChemElectroChem*, 2020, **8**, 291–336.

44 L. Y. Hu, *Preparation of Divalent Metal Ions Intercalated Manganese Dioxide for Supercapacitors*, Beijing University of Chemical Technology, 2021, in Chinese.

45 W. L. Xie, Design and synthesis of manganese dioxide-based electrode materials and their performance for energy storage, Lanzhou University, 2021.

46 B. Xu, H. Zhang, H. Mei, *et al.* Recent progress in metal-organic framework-based supercapacitor electrode materials, *Coord. Chem. Rev.*, 2020, **420**, 213438.

47 Y. Wang, X. Lin, T. Liu, *et al.* Wood-derived hierarchically porous electrodes for high-performance all-solid-state supercapacitors, *Adv. Funct. Mater.*, 2018, **28**, 1806207.

48 Q. Zhang, Z. Liu, B. Zhao, *et al.* Design and understanding of dendritic mixed-metal hydroxide nanosheets@N-doped carbon nanotube array electrode for high-performance asymmetric supercapacitors, *Mater. Today Energy Stor. Mater.*, 2019, **16**, 632–645.

49 H. Zhao, R. Jiang, Y. Zhang and etal, An MnO_2 nanosheet@nitrogen-dopcd graphene aerogel enables high specific energy and high specific power for supercapacitors and Zn-air batteries, *J. Mater. Chem. A*, 2021, **9**(9), 5848–5856.

50 P. T. Nguyen, J. Jang, Y. Lee and etal, Laser-assisted fabrication of flexible monofilament fiber supercapacitors, *J. Mater. Chem. A*, 2021, **9**(8), 4841–4850.

51 J. M. Jeong, S. H. Park, H. J. Park, *et al.*, Altenative-ultrathin assembling of exfoliated manganese dioxide and nitrogen-doped carbon layers for high-mass-loading supercapacitors with outstanding capacitance and impressive rate capability, *Adv. Funct. Mater.*, 2021, 2009632.

52 R. Chen, X. Li, Q. Huang, *et al.*, Self-assembled porous biomass caibon/rGO/nanocellulose hybrid aerogels for self-supporting supercapacitor electrodes, *Chem. Eng. J.*, 2021, **412**, 128755.

53 H. Yi, A. Gao, X. Pang and etal, Preparation of single-atom Ag-decorated MnO_2 hollow microspheres by redox etching method for high-performance solid-state asymmetric supercapacitors, *ACS Appl. Energy Mater.*, 2020, **3**(10), 10192–10201.

54 S. M. Jadhav, R. S. Kalubarme, N. Suzuki and etal, Cobalt-doped Manganese dioxide hierarchical nanostructures for enhancing pseudocapacitive properties, *ACS Omega*, 2021, **6**, 5717–5729.

55 Q. C. Xu, L. Y. Zhang, J. H. Zhang, J. Y. Wang, Y. J. Hu, H. Jiang and C. Z. Li, Anion Exchange Membrane Water Electrolyzer: Electrode Design, Lab-Scaled Testing System and Performance Evaluation, *EnergyChem*, 2022, **4**(5), 100087.

56 W. T. Li, X. T. Guo, P. B. Geng, M. Du, Q. L. Jing, X. D. Chen, G. X. Zhang, H. P. Li, Q. Xu, B. Pierre and H. Pang, Rationa-l Design and General Synthesis of Multimetallic Metal-Organic Framework Nano-Octahedra for Enhanced Li-S Battery, *Adv. Mater.*, 2021, **33**, 2105163.

57 Z. P. Ma, L. K. Fan, F. Y. Jing, *et al.* MnO_2 nanowires@NiCo-LDH nanosheet core-shell heterostructure: A slow irreversible transition of hydrotalcite phase for high-performance pseudocapacitance electrode, *ACS Appl. Energy Mater.*, 2021, **4**(4), 3983–3992.

58 S. Zhu, L. Li, J. Liu, *et al.* Structural directed growth of ultrathin parallel bimcssite on β-MnO_2 for high-performance asymmetric supercapacitors, *ACS Nano*, 2018, **12**(2), 1033–1042.

59 W. Liu, H. Huang, Z. Jiang, *et al.* Interfacial Titanium diffusion self-adapting layer in ultrathin epitaxial MnO_2/TiO_2 heterostructures, *ACS Appl. Mater. Interfaces*, 2020, **12**, 47010–47017.

60 L. Hu, R. Gao, A. Zhang, *et al.* Cu^{2+}intercalation activates bulk redox reactions of MnO_2 for enhancing capacitive performance, *Nano Energy*, 2020, **74**, 104891.

61 Y. Zhang, Y. Liu, Z. Sun and etal, Strategic harmonization of surface charge distribution with tunable redox radical for high-performing MnO_2-based supercapacitor, *Electrochim. Acta*, 2021, **375**, 137979.

62 Q. Chen, J. Jin, Z. Kou and etal, Zn^{2+} pre-intercalation stabilizes the tunnel structure of MnO_2 nanowires and enables zinc-ion hybrid supercapacitor of battery-level energy density, *Small*, 2020, **16**(14), 2000091.

63 Y. Bai, C. L. Liu, T. T. Chen, W. T. Li, S. S. Zheng, Y. C. Pi, Y. S. Luo and H. Pang, MXene-Copper/Cobalt Hybrids via Lewis Acidic Molten Salts Etching for High Performance Symmetric Supercapacitors, *Angew. Chem., Int. Ed.*, 2021, **60**, 25318.

64 S. S. Zheng, Q. Li, H. G. Xue, H. Pang and Q. Xu, A highly alkaline-stable metal oxide@metal–organic framework composite for high-performance electrochemical energy storage, *Natl. Sci. Rev.*, 2020, **7**, 305–314.

65 A. Zhang, R. Gao, L. Hu and etal, Rich bulk oxygen vacancies-engineered MnO_2 with enhanced charge transfer kinetics for supercapacitor, *Chem. Eng. J.*, 2021, **417**, 129186.

66 Y. Chen, C. Zhou, Q. Liu and etal, Hydroxide ion dependent α-MnO_2 enhanced via oxygen vacancies as the negative electrode for high-performance supercapacitors, *J. Mater. Chem. A*, 2021, **9**(5), 2872–2887.

67 W. Guo, C. Yu, S. Li, Z. Wang, J. Yu, H. Huang and J. Qiu, Strategies and insights towards the intrinsic capacitive properties of MnO_2 for supercapacitors: challenges and perspectives, *Nano Energy*, 2019, **57**, 459–472.

68 J. Zhu, R. Benages-Vilau and P. Gomez-Romero, Can polyoxometalates enhance the capacitance and energy density of activated carbon in organic electrolyte supercapacitors?, *Electrochim. Acta*, 2020, **362**, 137007.

69 A. Baral, L. Satish, G. Zhang, S. Ju and M. K. Ghosh, A review of recent progress on nano MnO_2: synthesis, surface modification and applications, *J. Inorg. Organomet. Polym. Mater.*, 2020, **31**(3), 899–922.

70 Y. Cao, K. Han, Z. Teng, J. Li, T. Ji, X. Li and J. Zhang, Optimized synergistic preparation of nitrogen-doped porous carbon derived from gasified carbon for supercapacitors, *J. Alloys Compd.*, 2021, **860**, 158385.

71 J. Noh, C. M. Yoon, Y. K. Kim and J. Jang, High performance asymmetric supercapacitor twisted from carbon fiber/MnO_2 and carbon fiber/MoO_3, *Carbon*, 2017, **116**, 470–478.

72 Y. Wang, W. Lai, N. Wang, Z. Jiang, X. Wang, P. Zou, Z. Lin, H. Fan, F. Kang, C. Wong and C. Yang, A reduced graphene oxide/mixed-valence manganese oxide composite electrode for tailorable and surface mountable supercapacitors with high capacitance and super-long life, *Energy Environ. Sci.*, 2017, **10**(4), 941–949.

73 P. Simon and Y. Gogotsi, Perspectives for electrochemical capacitors and related devices, *Nat. Mater.*, 2020, **19**(11), 1151–1163.

74 S. Kumar, G. Saeed, L. Zhu, K. N. Hui, N. H. Kim and J. H. Lee, 0D to 3D carbon-based networks combined with pseudocapacitive electrode material for high energy density supercapacitor: A review, *Chem. Eng. J.*, 2021, **403**, 126352.

75 X. Long, L. Tian, J. Wang, L. Zhang, Y. Chen, A. Emin, W. Xie, X. Wang, D. Liu, Y. Fu, J. Li, Y. Li and D. He, Interconnected δ-MnO_2 nanosheets anchored on activated carbon cloth as flexible electrode for high-performance aqueous asymmetric supercapacitors, *J. Electroanal. Chem.*, 2020, **877**, 114656.

76 S. Dang, Y. Wen, T. Qin, J. Hao, H. Li, J. Huang, D. Yan, G. Cao and S. Peng, Nanostructured manganese dioxide with adjustable Mn^{3+}/Mn^{4+} ratio for flexible high-energy quasi-solid supercapacitors, *Chem. Eng. J.*, 2020, **396**, 125342.

77 T. Qin, B. Liu, Y. Wen and etal, Freestanding flexible graphene foams@polypyrrole@MnO_2 electrodes for high-performance supercapacitors, *J. Mater. Chem. A*, 2016, **4**(23), 9196–9203.

78 X. J. Pu, D. Zhao, C. L. Fu, Z. X. Chen, S. N. Cao, C. S. Wang and Y. L. Cao, Understanding and Calibration of Charge Storage Mechanism in Cyclic Voltammetry Curves, *Angew. Chem., Int. Ed.*, 2021, **60**, 21310–21318.

79 A. Q. Zhang, R. Gao, L. Y. Hu, X. G. Zang, R. Yang, S. Y. Wang, S. Y. Yao, Z. Y. Yang, H. G. Hao and Y. M. Yan, Rich bulk oxygen Vacancies-Engineered MnO_2 with enhanced charge transfer kinetics for supercapacitor, *Chem. Eng. J.*, 2021, **417**, 1385–8947.

80 W. J. Yang, Y. F. Zhu, Y. Fei, L. Yan, Y. J. Ma, C. Y. Lu, P. Q. Gao, Q. Hao and W. L. Li, Insights into the Surface-Defect Dependence of Molecular Oxygen Activation over Birnessite-type MnO_2, *Appl. Catal., B*, 2018, **233**(37), 184–193.

81 Y. Jiang and J. Liu, Definitions of Pseudocapacitive Materials: A Brief Review, *Energy Environ. Mater.*, 2019, **2**, 30–37.